Chemical Insights into the Formation of Colloidal High Entropy Alloy Nanoparticles

Gaurav R. Dey,[1] Connor R. McCormick,[1] Samuel S. Soliman,[1] Albert J. Darling,[1] and Raymond E. Schaak[1,2,3,*]

[1] *Department of Chemistry,* [2] *Department of Chemical Engineering, and* [3] *Materials Research Institute, The Pennsylvania State University, University Park, PA 16802, United States.*

E-mail: res20@psu.edu

ABSTRACT

Nanoparticles of high entropy alloys (HEAs) have distinct properties that result from their high surface-to-volume ratios coupled with synergistic interactions among their five or more constituent elements, which are randomly distributed throughout a crystalline lattice. Methods to synthesize HEA nanoparticles are emerging, including solution approaches that yield colloidal products. However, the complex multi-element compositions of HEA nanoparticles make it challenging to identify and understand their reaction chemistry and the pathways by which they form, which hinders their rational synthesis. Here, we demonstrate the synthesis and elucidate the reaction pathways of seven colloidal HEA nanoparticle systems that contain various combinations of noble metals (Pd, Pt, Rh, Ir), 3d transition metals (Ni, Fe, Co), and a p-block element (Sn). The nanoparticles were synthesized by slowly injecting a solution containing all five constituent metal salts into oleylamine and octadecene at 275 ºC. Using NiPdPtRhIr as a lead system, we confirmed the homogeneous co-localization of all five elements and achieved tunable compositions by varying their ratios. We also observed heterogeneities, including Pd-rich regions, in a subpopulation of the NiPdPtRhIr sample. Halting the reaction at early time points and characterizing the isolated products revealed a time-dependent composition evolution from Pd-rich NiPd seeds to the final NiPdPtRhIr HEA. Similar reactions applied to FePdPtRhIr, CoPdPtRhIr, NiFePdPtIr, and NiFeCoPdPt, with modified conditions to most efficiently incorporate all five elements into each HEA, also revealed similar Pd-rich seeds with system-dependent differences in the rates and sequences of element uptake into the nanoparticles. When moving to SnPdPtRhIr and NiSnPdPtIr, the time-dependent formation pathway was more consistent with simultaneous co-reduction rather than through formation of reactive seeds. These studies reveal important similarities and differences among the pathways by which different colloidal HEA nanoparticles form using the same synthetic method, as well as establish generality. The results provide guidelines for incorporating a range of different elements into HEA nanoparticles, ultimately providing fundamental knowledge about how to define and optimize synthetic protocols, expand into different HEA nanoparticle systems, and achieve high phase purity.

KEYWORDS

High entropy alloys, nanoparticles, nanochemistry, nanomaterials, reaction pathways

INTRODUCTION

High entropy alloys (HEAs), which are generally considered to have five or more principal elements in near-equimolar ratios randomly distributed throughout a crystalline lattice,[1,2] have properties that differ from their constituent elements and simpler alloys. Synergistic interactions among the large number of elements in HEAs leads to exceptional mechanical properties,[3,4] as well as enhanced performance as thermoelectric,[5] magnetic,[6] and catalytic materials.[7,8] Some of these properties of HEAs can be further enhanced, or utilized in different ways, as nanoparticles. HEA nanoparticles have become especially high-value targets for their enhanced catalytic properties due to the so-called cocktail effect that arises from synergistic interactions among the elements, as well as improvements in activity, selectivity, and stability that emerge from the variety of chemical and electronic environments that is present.[7,9]

The formation of bulk HEAs is typically driven by the large configurational entropy associated with randomly mixing such a large number of elements on a crystalline lattice.[1] In HEAs, the configurational entropy overrides the enthalpic penalties of mixing at the high temperatures needed to synthesize them (>1000 ºC), which turns the free energy landscape negative.[1] Rapid quenching to room temperature is usually required to trap the HEA phase that is stabilized at high temperatures, where the $T\Delta S$ term of Gibbs free energy ($\Delta G = \Delta H - T\Delta S$) is large.[1] These synthetic requirements pose a problem for the synthesis of nanoparticles, which generally require low temperatures to minimize growth and to maintain nanoscopic dimensions.

Strategies have emerged for the synthesis of HEA nanoparticles. Among the most prominent method to synthesize HEA nanoparticles is carbothermal shock, where carbon-supported metal salt mixtures are rapidly heated to ~2000K and then cooled at a rate of 10^5 K/s.[10] Other techniques that have yielded nanoparticles of HEAs, as well as of multiprincipal element alloys and complex solid solutions (which differ from HEAs primarily in their definitions but colloquially still fall under the broad category of HEAs),[9] include kinetically controlled laser synthesis,[11,12] ultrasonication-assisted wet chemistry,[13] sputtering deposition,[14] spray pyrolysis,[15] and solution combustion.[16] While powerful, these techniques operate at very high temperatures, often require sophisticated setups, have limited scalability, and can hinder control over size and shape, which are important property-relevant parameters, especially for catalytic nanoparticles.

Solution-based colloidal syntheses are among the most powerful for nanoparticles, as they can facilitate the controlled nucleation and growth of solids through chemical or thermal triggers and can allow for exquisite control over size and shape while offering liquid dispersibility and processing, as well as the potential for scalability.[17,18] Significant advances over the past two decades have provided detailed chemical insights into the reactions that produce metal and simple alloy nanoparticles, and especially noble metal systems.[19,20,21] As a result, it is now possible to synthesize hundreds of different types of metal and alloy nanoparticles in solution with a high degree of control over size and shape. In contrast, methods to synthesize colloidal HEA nanoparticles are only beginning to emerge.[22,23,24,25] Additionally, little is known about the reaction chemistry that leads to their formation, given the large number of elemental reagents and their range of chemical reactivities, both individually and together.[26,27,28,29] Methods that sidestep the complex reaction chemistry by pre-designing heterostructured nanoparticle precursors and annealing them to form HEAs provide promising alternatives, but still require the particles to be anchored on refractory supports and annealed at high temperatures.[24,30]

To date, only a small number of reports describe the direct solution synthesis of unsupported colloidal HEA nanoparticles.[22,23,25,26,28,31,32,33,34,35,36] These reports generally approach the synthesis of colloidal HEA nanoparticles by simultaneously injecting five or more metal salts into

a solvent, either pre-heated or at room temperature prior to heating, as such methods are analogous to those used to synthesize high quality nanoparticles of the constituent metals and their simpler alloys. For these reactions, it is generally accepted that in most cases, all of the constituent metals co-reduce simultaneously and directly form HEA nanoparticles, given the high reaction temperatures and rapid kinetics. However, little is known about how key reaction variables influence colloidal HEA nanoparticle formation or stability. Even less is known about the reaction pathways that lead to their formation, as well as how reaction insights from one HEA nanoparticle system can be transferred to other systems.[25,26,27,28] Some mechanistic insights into the formation of HEA nanoparticles are emerging, but they generally involve different synthetic approaches that do not map onto the types of reactions that are most commonly used to make colloidal HEAs.[24,26,27] These knowledge gaps limit the rational synthesis of colloidal HEA nanoparticles, which is a significant shortcoming given the rapidly growing interest in the properties and applications of these materials.

Here, we demonstrate the direct solution-based synthesis of colloidal HEA nanoparticles that contain noble and non-noble metals using a straightforward hot-injection approach that aligns with mainstream methods for synthesizing metal and simpler alloy nanoparticles. Using NiPdPtRhIr as a strategic model system, we probe the reaction pathway to gain insights into the steps that transform dissolved metal salts into HEAs. Through these studies, we identify intermediate nanoparticle species that are implicated in HEA formation, and therefore rule out the simultaneous co-reduction pathway that is most often considered to be operable in HEA nanoparticle synthesis. We then compared and contrasted these results with related systems, FePdPtRhIr and CoPdPtRhIr, having different non-noble metals. We then moved to derivatives containing two (NiFePdPtIr) and three (NiFeCoPdPt) non-noble metals, as well as a p-block element without (SnPdPtRhIr) and with (NiSnPdPtIr) a non-noble metal. The Sn-based HEAs are particularly instructive, as they are found to form through a pathway that is distinct from the pathway by which the all-transition metal systems form. These similarities and differences among the pathways by which different colloidal HEA nanoparticles form using the same synthetic method provide guidelines for incorporating a range of different noble metals, non-noble metals, and p-block elements into colloidal HEA nanoparticles. These studies also establish the viability of the synthetic method, demonstrate generality, and define strategies for optimizing synthetic protocols for expanding into different HEA nanoparticle systems to achieve high phase purity. These capabilities are an important prerequisite for the rational synthesis of compositionally complex nanoparticles that are emerging as high-value targets for a growing scope of applications.

RESULTS AND DISCUSSION

Synthesis and Characterization of NiPdPtRhIr

Our general protocol for synthesizing colloidal HEA nanoparticles involves slowly injecting a dilute precursor solution containing each of the five metal salts into a preheated solvent mixture. This synthetic methodology is well established in the metal and alloy nanoparticle synthesis literature[37] but had to be modified and optimized to facilitate HEA formation, as discussed below. The key parameter is the slow injection of a dilute precursor mixture, which minimizes the frequency of collisions between atoms of the same elements to avoid formation of individual metal nanoparticles while maximizing the frequency of collisions between atoms of different elements to favor formation of HEA nanoparticles.

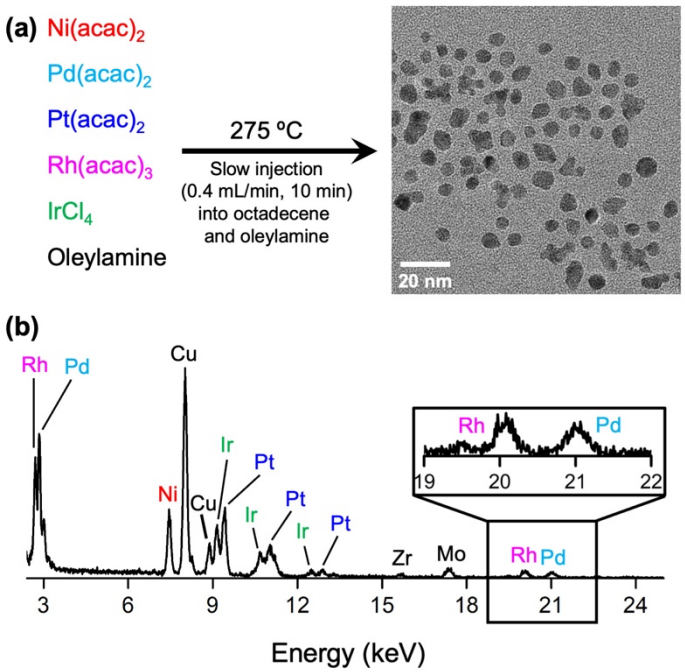

Figure 1. Synthesis of NiPdPtRhIr nanoparticles and characterization by TEM and EDS. (a) Protocol for the synthesis of NiPdPtRhIr nanoparticles and the corresponding TEM image showing their morphology and size. (b) EDS spectrum confirming the presence of all five elements (Ni, Pd, Pt, Rh, Ir). The Cu signal is from the Cu TEM grid, the Mo signal is from the Mo clips used in the TEM holder, and Zr is from the instrument.

We began by studying the formation of NiPdPtRhIr, a representative HEA containing one non-noble metal and four noble metals. Nanoparticles of NiPdPtRhIr were synthesized by injecting 4 mL of a precursor solution containing 0.8 mL each of 10.54 mM $Ni(acac)_2$, $Pd(acac)_2$, $Pt(acac)_2$, $Rh(acac)_3$, and $IrCl_4$, dissolved in oleylamine, over 10 minutes at a rate of 0.4 mL/min, into octadecene and oleylamine at 275 °C. Figure 1a shows a TEM image of the NiPdPtRhIr nanoparticles, which are nominally spherical and/or multi-faceted and range in diameter from approximately 5 – 10 nm, with an average diameter of less than 10 nm. Figure S1 shows a HRTEM image, which highlights the crystallinity of the nanoparticles. Figure 1b, which shows a corresponding EDS spectrum for an ensemble of particles, indicates that all five metals are present. The composition of the sample, as determined from the EDS spectrum, is $Ni_{0.19}Pd_{0.21}Pt_{0.22}Rh_{0.20}Ir_{0.18}$, which matches well with the nominal 1:1:1:1:1 ratios of the precursor solution. Figure 2a shows powder XRD patterns for the NiPdPtRhIr nanoparticles, along with a reference pattern that was constructed based on a face centered cubic (fcc) alloy having a lattice parameter of a = 3.83 Å. This value compares favorably with the weighted average (based on the nominal composition) of the lattice parameters of the constituent fcc metals, which is a = 3.796 Å; details of lattice constants and weighted average calculations are provided in the Supporting Information (Table S1). The experimental XRD pattern is consistent with a phase-pure HEA nanoparticle sample without any additional crystalline impurities or evidence of significant amorphous material.

The composition of the NiPdPtRhIr nanoparticles can be systematically varied by changing the ratios of the constituent elements, offering wide tunability. To demonstrate, the amount of one of the five elements was increased to 40% (in bold below) while the other four elements were restricted to 15%. Figure 2b shows the powder XRD patterns for the products with nominal

compositions of **$Ni_{0.40}$**$Pd_{0.15}Pt_{0.15}Rh_{0.15}Ir_{0.15}$, $Ni_{0.15}$**$Pd_{0.40}$**$Pt_{0.15}Rh_{0.15}Ir_{0.15}$, $Ni_{0.15}Pd_{0.15}$**$Pt_{0.40}$**$Rh_{0.15}Ir_{0.15}$, $Ni_{0.15}Pd_{0.15}Pt_{0.15}$**$Rh_{0.40}$**$Ir_{0.15}$, and $Ni_{0.15}Pd_{0.15}Pt_{0.15}Rh_{0.15}$**$Ir_{0.40}$**. The peak positions for each of these alloys were shifted slightly, which is expected for changes in composition.

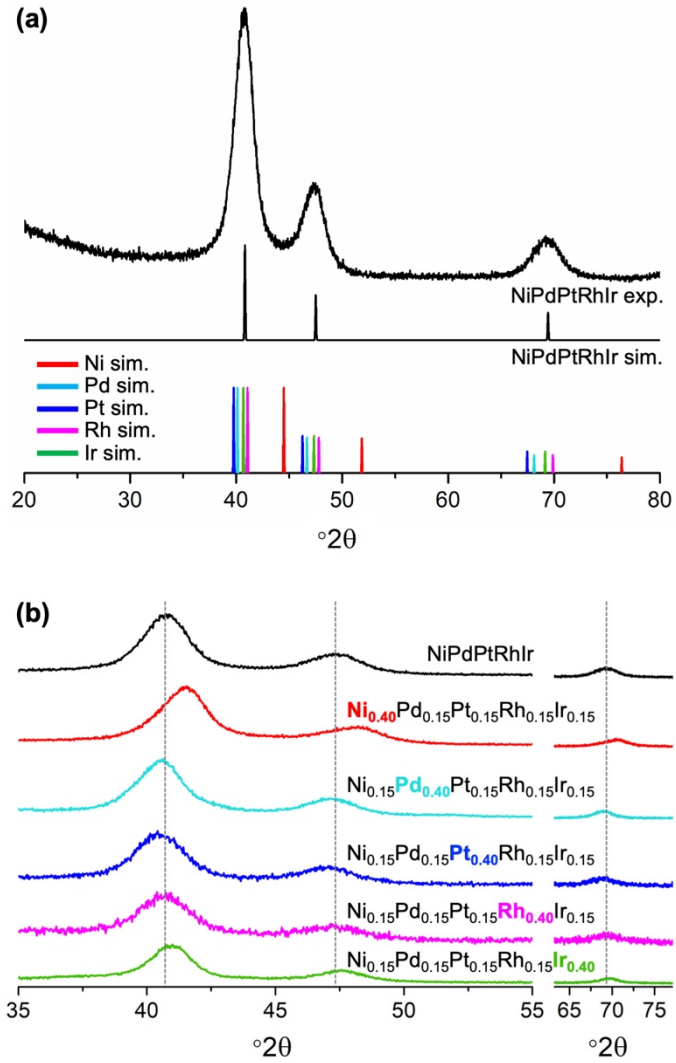

Figure 2. Powder XRD data (Cu Kα radiation) characterization of NiPdPtRhIr nanoparticles. (a) Experimental XRD pattern for $Ni_{0.19}Pd_{0.21}Pt_{0.22}Rh_{0.20}Ir_{0.18}$ nanoparticles, along with a simulated fcc XRD pattern for NiPdPtRhIr using a = 3.83 Å. Reference XRD patterns for each individual element is provided for reference. A detailed description of how the simulated patterns were generated is provided in the Supporting Information. (b) XRD patterns for compositionally varied NiPdPtRhIr samples. Regions from 35-55 º2θ and 65-75 º2θ are shown, and the gray dashed lines highlight the shifting of the peaks. Each sample has one element at 40% and the other four at 15%.

Figure 3a shows STEM-EDS element maps of a representative NiPdPtRhIr nanoparticle; data for a collection of nanoparticles is shown in Figure 3b. The data in Figures 3a and 3b confirm that the five metals are colocalized and homogeneously distributed within the nanoparticles. Figure 3c and S2 shows STEM-EDS data, along with an accompanying line scan in Figure 3d, for a different region of the sample, which corresponds to a minority subpopulation of particles that were observed. Here, some compositional heterogeneity is observed, including a particle with a

Pd-rich core. Such heterogeneity is not unexpected, given the many ways in which five metals can mix.[30] However, because we consistently observe Pd-rich regions in some of the NiPdPtRhIr nanoparticles, we decided to investigate how and why this specific type of heterogeneity is so prominent.

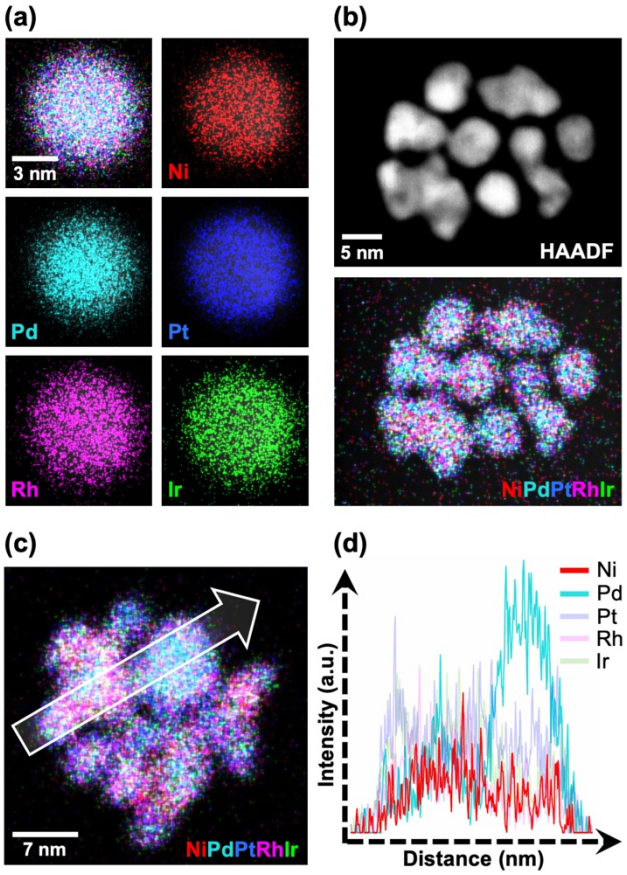

Figure 3. Microscopy characterization of NiPdPtRhIr nanoparticles. (a) An overlaid STEM-EDS element map along with individual STEM-EDS element maps (Ni Kα, red; Pd Lα, cyan; Pt Lα, blue; Rh Lα, pink; Ir Lα, green) for a single $Ni_{0.19}Pd_{0.21}Pt_{0.22}Rh_{0.20}Ir_{0.18}$ nanoparticle. (b) HAADF-STEM image and the corresponding overlaid STEM-EDS element map for an ensemble of $Ni_{0.19}Pd_{0.21}Pt_{0.22}Rh_{0.20}Ir_{0.18}$ nanoparticles. (c) Overlaid STEM-EDS element map for a different region of the same sample showing regions with high Pd concentration and (d) a line scan through the region marked with an arrow in (c). The line scan covers a total distance (x-axis) of 18 nm.

Reaction Pathway for NiPdPtRhIr

A typical synthesis of NiPdPtRhIr nanoparticles involves slowly injecting, over 10 minutes, the dilute precursor solution that contains all five dissolved metal reagents. To begin probing how the NiPdPtRhIr nanoparticles form, we carried out a series of time-dependent studies by synthesizing samples where the five-metal precursor solution injection was halted after 1 min, 2.5 min, 5 min, and 7.5 min, in addition to the 10-minute sample. (The concentrations and injection rates remain the same, so the different injection times correspond to different overall amounts of metal reagents added, with all other conditions, including ratios of metals, remaining the same.) Figure 4 shows STEM-EDS element maps for representative samples; additional STEM-EDS element maps are shown in Figure S3. Analysis of the compositions of multiple regions of particles (Figure S4) confirms that the trends in Figure 4 apply regardless of the subpopulations imaged. Figure 4

also shows quantitatively how the ratios of the various elements fluctuate as the HEA formation reaction proceeds. Analysis of these data, along with the corresponding STEM-EDS maps that show the transformation of compositionally heterogenous particles into a more homogeneous system, provides chemical insights into the pathways by which the HEA nanoparticles form.

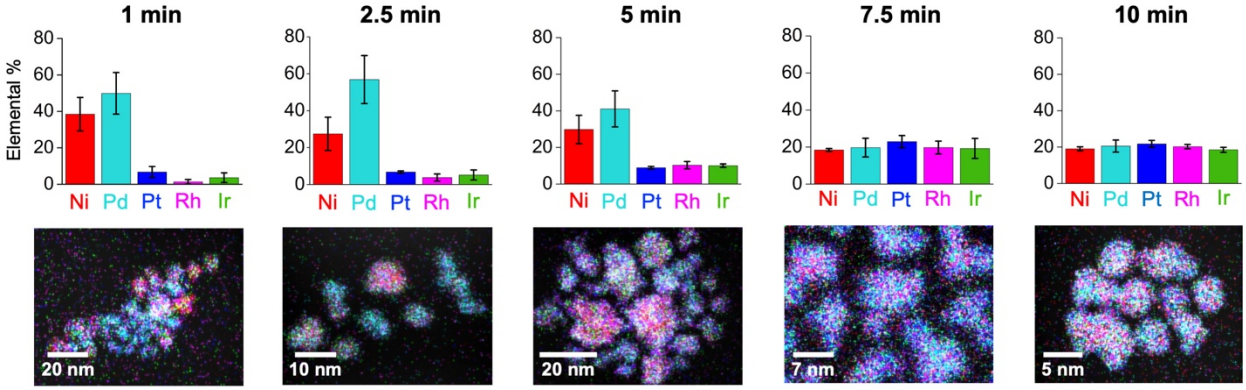

Figure 4. Time-dependent formation of NiPdPtRhIr nanoparticles. Bar charts showing elemental composition (obtained from EDS measurements) and corresponding STEM-EDS element maps for samples of NiPdPtRhIr nanoparticles isolated at various times during the slow-injection synthesis (Ni Kα, red; Pd Lα, cyan; Pt Lα, blue; Rh Lα, pink; Ir Lα, green).

Analysis of the data in Figure 4 characterizing the time-dependent evolution of nanoparticle composition provides important mechanistic clues into how the reaction proceeds from dissolved metal salts to HEA nanoparticles. The particles that form within the first minute of the reaction are visibly heterogeneous, consisting primarily of Pd-rich Pd-Ni seeds. By 2.5 minutes, the Pd-rich Pd-Ni seeds still exist, but the average Pd content increases slightly while the Ni content decreases concomitantly; the other elements begin to incorporate into the particles, although in very low amounts. Some Ni-rich particles can also be observed in the STEM-EDS element maps. By 5 minutes, the average Pd content decreases as the amounts of Pt, Rh, and Ir increase; the average Ni content does not change significantly. By 7.5 minutes, the amounts of Pd and Ni have significantly decreased and the amounts of Pt, Rh, and Ir have significantly increased, together leading to a near-equimolar ratio of Ni:Pd:Pt:Rh:Ir. At this point, the composition remains constant, not changing significantly between 7.5 and 10 minutes. It is worth noting that control studies show $Pd(acac)_2$, $Pt(acac)_2$, and $Ni(acac)_2$ in oleylamine, under the conditions used to synthesize the HEA nanoparticles, form Pd, Pt, and Ni nanoparticles, respectively, at different rates, as observed visually as the reactions progress. Pd is observed to reduce the fastest, followed by Pt, even though Pt has a more positive reduction potential. Attempts were made to form Pd/NiPd seeds *in situ*, followed by addition of other metals to encourage a seed-mediated growth process, but such reactions did not form phase-pure HEAs containing all five metals.

Based on the data in Figures 3 and 4, we can now describe the pathway by which NiPdPtRhIr nanoparticles form. The reaction begins initially with the formation of PdNi nanoparticles, which is important for the autocatalytic and redox processes to initiate later. PdNi nanoparticles, when decomposed from acetylacetonate salts, are known in the literature to form a $Pd_{core}@Ni_{shell}$ structure.[38,39] The presence of Pd-rich PdNi nanoparticles, with Pd concentrations highest in the center, hints at the possible initial, rapid formation of a Pd seed, followed by incorporation of Ni by deposition and diffusion. We do not observe Pd@Ni core-shell particles in our reaction, which is not unexpected due to the fast reaction kinetics and diffusion rates at such high temperatures. Pt has the third highest concentration in these intermediate nanoparticles after Pd and Ni,

suggesting that Pt starts to incorporate next after PdNi forms. It is well known in the literature that deposition of more noble metals can be triggered by galvanic replacement and concomitant alloying with less noble metals,[40] as would be the case for Pt vs. both Pd and Ni.[41,42] This observation suggests that Ni and/or Pd must be present for the Pt to incorporate into the nanoparticles, which is enabled by the PdNi nanoparticles that are observed first.

The potential importance of a Pd-rich intermediate was previously noted by Iversen and co-workers, who studied the *in situ* formation of PtIrPdRhRu HEA nanoparticles using a solvothermal reaction in a pressurized capillary system.[26] They found, for a different system than ours and for much larger particles and agglomerates, that HEA formation was autocatalyzed by the (111) facets of an initially formed Pd core onto which the other metals reduce at the expense of Pd, and also that homogeneous mixing of all five metals depended on the combined influences of both temperature and time.[26] For our NiPdPtRhIr system made using a more mainstream colloidal synthesis platform, the constituent metals are simultaneously added into the hot reducing solution rather than through a one-pot heat up method where different metal salts decompose and reduce at different temperatures and at different rates. In our case, all metal salts decompose simultaneously at the hot injection temperature, but with different rates of reduction. This allows details of the stepwise process to be uncovered, as evidenced by the initial formation of Pd-rich Pd-Ni nanoparticles into which Pt slowly diffuses in, followed by a possible similar autocatalytic process that results in the reduction and incorporation of Rh and Ir. Support for an autocatalytic process for incorporating Rh and Ir comes from the outcomes for attempted syntheses of nanoparticles of each individual metal using the slow injection method with identical reaction conditions. We observed that only Pd and Pt nanoparticles could be isolated from such reactions. Ni_3C nanoparticles formed *in lieu* of Ni nanoparticles under these reaction conditions while Rh and Ir nanoparticles did not form (Figure S5). Note that Rh nanoparticles can be synthesized by heating $Rh(acac)_3$ in oleylamine for one hour,[43] but our process that involves slow injection of $Rh(acac)_3$ over 10 minutes was insufficient to reduce and form Rh nanoparticles.

The slow-injection method enabled the reaction pathway to be studied at various time points. However, many types of colloidal nanoparticles are formed through rapid-injection methods. Therefore, using the same dilute concentrations, we also studied a rapid-injection synthesis of NiPdPtRhIr nanoparticles. Here, the same precursor solution mixture detailed earlier for the slow injection process was rapidly injected into the same solvent mixture of oleylamine and octadecene at 275 ºC. Particles isolated immediately after injection contained a very high concentration of Pd (~79%). Small amounts of Pt and Ni (~9% each), as well as Ir (~2%), were also present in these particles, while Rh was completely absent (Figures S6 and S7). Particles isolated 1 min after rapid injection had incorporated much more Ni (~30%), with the relative amount of Pd decreasing to ~52%. The particles isolated at 1 min therefore were NiPd-rich seeds; some Rh (~9%) was also incorporated. After 1 hour of heating at 275 ºC, the compositions of the nanoparticles throughout the sample were more homogeneous, as shown in Figures S6 and S7. However, sample-to-sample heterogeneity is evident and indicates that a slow injection is critical to ensure homogeneous mixing. Overall, the compositional evolution of the particles throughout the reactions, and the predominance of Ni and Pd early in the reaction, points to a similar overall pathway for both the slow-injection and rapid-injection methods.

The NiPdPtRhIr nanoparticles synthesized using both slow-injection and fast-injection methods were deposited on a silicon wafer, heated to 800 ºC under argon for 24 hours, and slow cooled in the furnace to room temperature (Figure S8). High entropy materials may be expected to phase segregate upon slow cooling if they are truly entropy stabilized, since entropy-driven transitions are known to be reversible. However, for both samples, the XRD patterns remained largely unchanged. This observation suggests that the NiPdPtRhIr nanoparticles may not be entropy

stabilized, which is not unexpected since they are synthesized in solution at temperatures below those at which the $T\Delta S$ term would be expected to be sufficiently large to drive entropic stabilization; the reaction pathway and chemistry facilitate their combination rather than configurational entropy. At the temperatures used for colloidal nanoparticle synthesis, the synthetic challenge is balancing chemical reactivity rather than maximizing the entropy of mixing. The driving force for colloidal HEA nanoparticle formation is therefore most likely to be enthalpic, based on balanced chemical reactivities for each element. Here, the Pd seed acts as a face centered cubic template for other metals to adopt, as well as an autocatalytic agent to facilitate the reduction of the other metal salts. We have also strategically chosen our alloy systems such that the constituent metals have similar sizes to favor diffusion and mixing rather than phase segregation. (It is important to note that based on convention in the field and terminology that is widely used in the literature, high entropy materials are considered to have at least five principal elements, each contributing 5% - 35% to the total atomic percentage, regardless of their stabilization. These, and many other so-called high entropy alloys, are more accurately described as multiprincipal element alloys or complex solid solutions,[9] but convention convolutes these definitions. We acknowledge these distinctions but generally still refer to them as HEAs based on current convention in the field.)

Incorporation of additional non-noble metals

The slow-injection synthesis of colloidal NiPdPtRhIr nanoparticles used in the previous section involved slowly injecting 4 mL of the five-metal precursor solution into a mixture of octadecene and oleylamine that was preheated to 275 ºC. Here, we applied these same reaction conditions to the synthesis of related HEA nanoparticles that contained different non-noble metals. Attempts to synthesize FePdPtRhIr using $Fe(acac)_3$ and CoPdPtRhIr using $Co(acac)_3$ – two commonly used Fe and Co reagents for synthesizing colloidal metal and alloy nanoparticles – resulted in incorporation of just 10% of Fe and Co, respectively, based on the EDS data in Figure S9. Moreover, the CoPdPtRhIr sample had a high Pd composition of ~47%. This result contrasts that for NiPdPtRhIr, which contained 19% Ni using $Ni(acac)_2$ under the same conditions. To incorporate more Fe and Co, we rapidly injected the precursor solution (instead of the slow injection method that was used for NiPdPtRhIr), increased the temperature to 315 ºC, and held for 1 hour to favor complete decomposition of the $Fe(acac)_3$ and $Co(acac)_3$.[25] As shown in Figure 5, both FePdPtRhIr and CoPdPtRhIr were synthesized as single-phase fcc HEAs, with the experimental pattern matching a reference pattern with a = 3.85 Å and a = 3.85 Å for FePdPtRhIr and CoPdPtRhIr, respectively. These values are very close to 3.823 Å (for FePdPtRhIr) and 3.804 Å (for CoPdPtRhIr), which are the weighted averages of the 1:1:1:1:1 nominal composition. The corresponding STEM-EDS element maps of the final products confirmed homogeneous incorporation of Fe and Co, respectively (Figures 5, S10 and S11). Analysis of the EDS data indicates average compositions of $Fe_{0.24}Pd_{0.16}Pt_{0.22}Rh_{0.18}Ir_{0.20}$ and $Co_{0.15}Pd_{0.31}Pt_{0.22}Rh_{0.14}Ir_{0.18}$, indicating that significantly more Fe and Co incorporated using the modified higher-temperature reaction conditions. The need for higher temperatures and longer reaction times can be traced back to the reaction conditions necessary to form Fe and Co nanoparticles. Certain metal acetylacetonate salts require a higher temperature to decompose while the different reduction potentials and reduction kinetics among the constituent salts lead to poor incorporation into the alloys.[25] This result indicates that the reaction conditions need to be adjusted to account for the decomposition and reduction kinetics of the most stable salt being used in the reaction to counter the varied reduction rates and ensure the availability of monomers in solution for autocatalytic reduction pathways to take over.

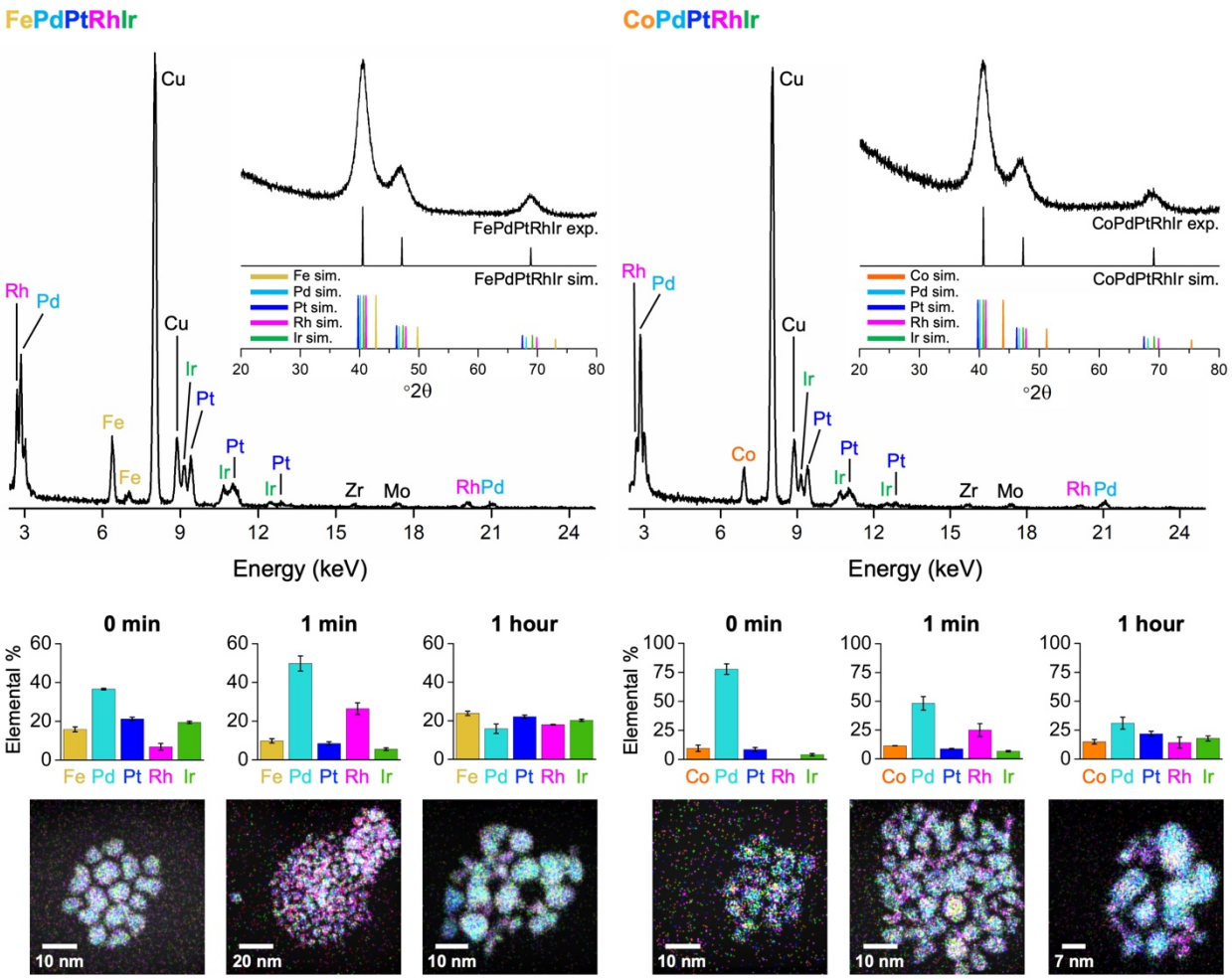

Figure 5. Characterization and time dependent formation of FePdPtRhIr and CoPdPtRhIr nanoparticles. Ensemble EDS spectra and powder XRD patterns (Cu Kα radiation) are shown at the top. The EDS spectra confirm the presence of all five elements in each sample. The Cu signal is from the Cu TEM grid, the Mo signal is from the Mo clips used in the TEM holder, and Zr is from the instrument. The XRD patterns confirm the formation of single-phase fcc alloys. Simulated fcc XRD patterns for each HEA, along with reference XRD patterns for each individual element, are provided for comparison. At the bottom, bar charts of EDS elemental composition are shown, along with corresponding STEM-EDS element maps (Fe Kα, yellow; Co Kα, orange; Pd Lα, cyan; Pt Lα, blue; Rh Lα, pink; Ir Lα, green). The time evolution of these systems is shown through the STEM-EDS maps, leading to nanoparticles having final compositions of $Fe_{0.24}Pd_{0.16}Pt_{0.22}Rh_{0.18}Ir_{0.20}$ and $Co_{0.15}Pd_{0.31}Pt_{0.22}Rh_{0.14}Ir_{0.18}$ by the end of one hour.

Analogous to NiPdPtRhIr, we studied early timepoints in the reactions that formed FePdPtRhIr and CoPdPtRhIr to gain insights into the pathways by which they form. Immediately after rapid injection at 315 ºC, *i.e.*, at a time of 0 min, the FePdPtRhIr HEA nanoparticles were Pd rich (~ 37%) and Rh poor (~ 7%) while the other three metals (Fe, Pt, Ir) were approximately equimolar (~16%, 21%, 19% each respectively). However, 1 min into the reaction, both the Pd and Rh concentration in the particles increased to 50% and 26%, respectively, with Fe, Pt, and Ir each comprising 10%, 8% and 6%, respectively. For CoPdPtRhIr under identical conditions, the particles isolated at 0 min are also highly Pd rich (~78%) and devoid of any Rh. Co and Pt have

very low incorporation (~9% each) while Ir is present at only ~4%. However, 1 min into the reaction, the Rh concentration increases significantly to ~25%, with Pd present at 48%. These data in Figures 5, S10, and S11 confirm that FePdPtRhIr and CoPdPtRhIr form through a pathway similar to that of NiPdPtRhIr, where a Pd-rich seed forms first and then Pt, Rh, Ir, and Fe or Co are subsequently incorporated.

To incorporate two and three non-noble metals, we targeted NiFePdPtIr and NiFeCoPdPt, respectively. Given the insights from the FePdPtRhIr and CoPdPtRhIr systems, we anticipated that higher temperatures (*i.e.*, 315 ºC *vs* 275 ºC) would favor incorporation of Fe and Co. Indeed, NiFePdPtIr and NiFeCoPdPt form best at 315 ºC. As shown in Figure 6, the EDS spectra indicate incorporation of all expected elements and the powder XRD data indicate the formation of single-phase alloys. For NiFePdPtIr, a = 3.80 Å, and for NiFeCoPdPt, a = 3.79 Å; these values compare favorably with the weighted averages of the constituent elements, which are a = 3.767 Å and a = 3.712 Å, respectively. The STEM-EDS element maps (Figures 6 and S12) indicate that NiFePdPtIr, which contains two non-noble metals, forms a single fcc HEA with the five constituent elements homogeneously distributed using the rapid-injection method at 315 ºC for 1 hour, identical to the protocol used to make FePdPtRhIr and CoPdPtRhIr. At lower temperatures or shorter reaction times, NiFePdPtIr still forms, but the composition distribution is inhomogeneous and/or only a small amount of Fe is incorporated. For NiFeCoPdPt, which contains three non-noble metals, a single fcc HEA with all five elements co-localized forms *via* slow injection at 315 ºC for 10 minutes (Figures 6 and S13), again reinforcing that the higher-temperature reaction facilitates incorporation of Fe and Co. At lower temperatures or shorter reaction times, either a Pd-rich core or inhomogeneities with NiPd-rich regions are observed, which suggests that the pathway operable for the formation of NiPdPtRhIr, which forms NiPd first, is operable for NiFeCoPdPt, with the other elements requiring higher temperatures or longer reaction times to incorporate.

Interestingly, while NiFeCoPdPt forms as a single fcc HEA at 315 ºC for 10 minutes, heating for 1 hour results in nanoparticles having very little Pd but very high amounts of Ni and Pt (Figure S14). This evolution from $Ni_{0.18}Fe_{0.22}Co_{0.17}Pd_{0.23}Pt_{0.20}$ to $Ni_{0.28}Fe_{0.19}Co_{0.18}Pd_{0.05}Pt_{0.30}$ (composition based on EDS data shown in Figure 6 and S14) between 10 minutes and 1 hour at 315 ºC is attributed to a redox equilibration process. Pd is less noble than Pt, based on standard reduction potentials (0.951 V for Pd^{2+}/Pd and 1.18 V for Pt^{2+}/Pt),[44] so it is possible that at this high temperature, more Pt deposits from solution as Pd in the nanoparticles sacrificially oxidizes. Similarly, Ni^{2+} (–0.257 V for Ni^{2+}/Ni)[44] would be expected to reduce while Co (1.92 V for Co^{3+}/Co^{2+} and –0.28 V for Co^{2+}/Co)[44] and Fe (0.771 V for Fe^{3+}/Fe^{2+} and –0.447 V for Fe^{2+}/Fe)[44] sacrificially oxidize, based on standard reduction potentials. (This same rationale also explains why there is always more Ni than Fe in the preceding system, NiFePdPtIr.) Thus, we rationalize the change in composition for the sample that is rich in non-noble metals as occurring due to the redox relationships that exist between the reduced metals in the HEA and residual metal salts still in solution. Interrogation of these systems therefore provides practical insights into predicting optimal synthetic conditions based on the reactivity relationships of the constituent elements.

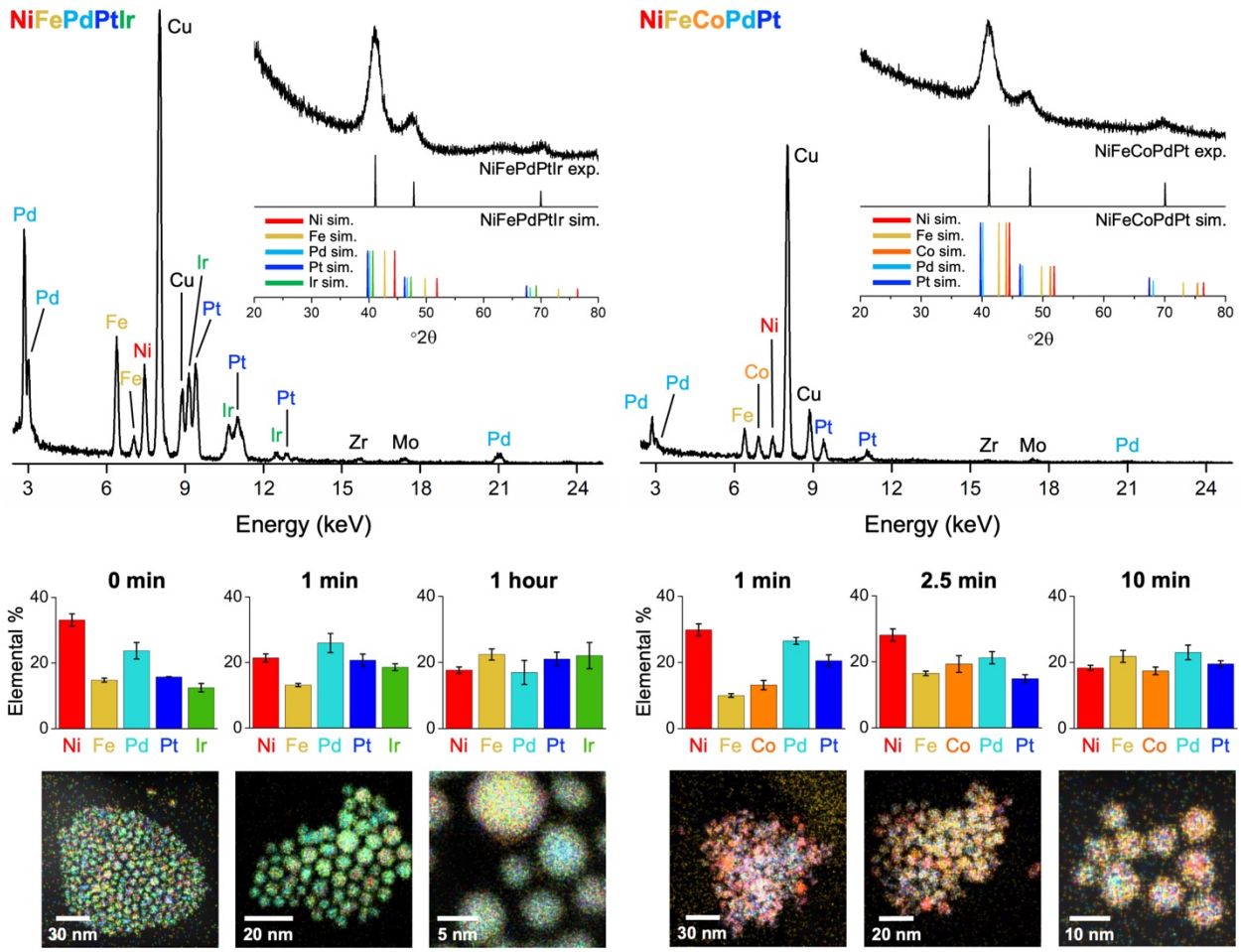

Figure 6. Characterization and time dependent formation of NiFePdPtIr and NiFeCoPdPt nanoparticles. Ensemble EDS spectra and powder XRD patterns (Cu Kα radiation) are shown at the top. The EDS spectra confirm the presence of all five elements in each sample. The Cu signal is from the Cu TEM grid, the Mo signal is from the Mo clips used in the TEM holder, and Zr is from the instrument. The XRD patterns confirm the formation of single-phase fcc alloys. Simulated fcc XRD patterns for each HEA, along with reference XRD patterns for each individual element, are provided for comparison. The small hump in the XRD pattern around 62 º2θ is an artifact from the XRD plate. At the bottom, bar charts of EDS elemental composition are shown, along with corresponding STEM-EDS element maps (Ni Kα, red; Fe Kα, yellow; Co Kα, orange; Pd Lα, cyan; Pt Lα, blue; Ir Lα, green). The time evolution of these systems is shown through the STEM-EDS maps, leading to nanoparticles having final compositions of $Ni_{0.18}Fe_{0.22}Pd_{0.17}Pt_{0.21}Ir_{0.22}$ and $Ni_{0.18}Fe_{0.22}Co_{0.17}Pd_{0.23}Pt_{0.20}$.

Incorporation of Sn (p-block element)

To our knowledge, Sn has not yet been incorporated into directly synthesized colloidal HEA nanoparticles. As a representative p-block element, we studied the synthesis of SnPdPtRhIr using the slow-injection method used to make NiPdPtRhIr and the other HEA nanoparticles described in the previous section. The powder XRD data for the product, shown in Figure 7, matches well with a single fcc phase. The lattice constant of SnPdPtRhIr, *a* = 3.95 Å, is significantly larger than that of the HEAs containing 3d transition metals, which ranged from *a* = 3.83 Å for NiPdPtRhIr to

a = 3.79 Å for NiFeCoPdPt, as expected given the larger size of Sn. However, unlike the other elements in our HEA alloy nanoparticles, elemental Sn does not adopt a stable fcc phase. Hence, a computed fcc Sn lattice constant of *a* = 4.81 Å[45] was used in calculating the predicted lattice constant of SnPdPtRhIr, which was *a* = 4.05 Å, based on a 1:1:1:1:1 weighted average. This calculated value is larger than the observed lattice constant of 3.95 Å, but is still qualitatively consistent with the large increase in unit cell size upon incorporation of Sn. An EDS spectrum and STEM-EDS element maps, also shown in Figure 7, indicate that all five elements are present and colocalized within the particles, therefore confirming a composition of $Sn_{0.25}Pd_{0.18}Pt_{0.23}Rh_{0.15}Ir_{0.19}$ with homogeneous distribution of the five elements.

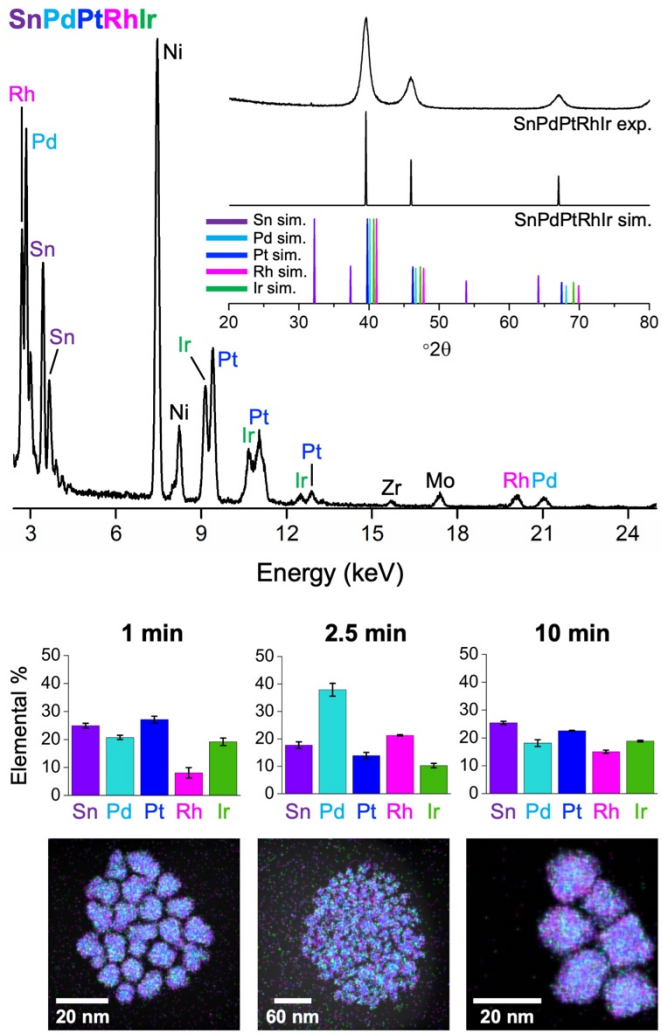

Figure 7. Characterization and time dependent formation of SnPdPtRhIr. An ensemble EDS spectrum and powder XRD pattern (Cu Kα radiation) are shown at the top. The EDS spectrum confirms the presence of all five elements in the sample. The Ni signal is from the Ni TEM grid, the Mo signal is from the Mo clips used in the TEM holder, and Zr is from the instrument. The XRD pattern confirms the formation of a single-phase fcc alloy. A simulated fcc XRD pattern, along with reference XRD patterns for each individual element, are provided for comparison. At the bottom, bar charts of EDS elemental composition are shown, along with corresponding STEM-EDS element maps (Sn Lα, purple; Pd Lα, cyan; Pt Lα, blue; Rh Lα, pink; Ir Lα, green). The time evolution is shown through the STEM-EDS maps, leading to nanoparticles having a final composition of $Sn_{0.25}Pd_{0.18}Pt_{0.23}Rh_{0.15}Ir_{0.19}$.

As for NiPdPtRhIr, we halted the reaction at early time points to gain insights into the pathway by which the SnPdPtRhIr nanoparticles form. Figure 7 shows STEM-EDS element maps for the particles formed after 1 minute and after 2.5 minutes. At 10 minutes, the particles are much larger in size, ~15 nm, compared to NiPdPtRhIr, and also compositionally homogeneous as evident from the STEM-EDS map in Figures 7 and S15. Sn incorporation in these nanoparticles is consistently higher relative to the other metals while Rh is lower, but both still fall within the accepted definition of HEAs. Unlike for NiPdPtRhIr, for SnPdPtRhIr there is no evidence of a Pd-rich seed that forms first. Instead, all elements were present, even in the 1-minute sample, in nearly equal proportions, although the nanoparticles were consistently deficient in Rh relative to the other elements. These results suggest that SnPdPtRhIr forms through a different pathway than the systems containing only transition metals.

Since the STEM-EDS data taken from the early time points seemed to rule out the seed-mediated pathway adopted by the all-transition metal systems, we considered the possibility of an alternate pathway for the Sn-containing HEA. To gain insights, we carried out two experiments that separated the simultaneous injection into stepwise reactions. In the first experiment, we rapidly injected $SnCl_2$ in oleylamine into the flask containing oleylamine and octadecene at 275 ºC and held for 2 minutes, followed by slowly injecting 4 mL of a solution of the other four metal salts [10.54 mM each of $Pd(acac)_2$, $Pt(acac)_2$, $Rh(acac)_3$, and $IrCl_4$] over 10 minutes. After the rapid injection of $SnCl_2$ into the heated solvent, the color of the solution did not change, suggesting that Sn nanoparticles did not form. (Sn is metallic, so the presence of Sn nanoparticles would cause the solution to turn a darker color.) However, nanoparticles did indeed form immediately after injection of the Pd, Pt, Rh, and Ir salt solution into the heated Sn salt solution. XRD data for the nanoparticle product shows a single-phase fcc alloy, and the STEM-EDS element maps in Figures S16 and S17 confirm that they contain all five elements, homogeneously distributed throughout the particles, albeit low in Rh. In the second experiment, we slowly injected the Pd, Pt, Rh, and Ir salt solution into the heated solvent at 275 ºC, followed by rapid injection of the $SnCl_2$ solution and holding for 2 minutes before stopping the reaction when it is at 200 ºC by quenching with water; particles appeared to form immediately upon injecting the noble metal salts, based on a rapid change in the color of the solution from colorless to black while injection of the $SnCl_2$ did not result in any visible color change. Again, XRD data shows a single-phase fcc alloy and STEM-EDS element maps confirm homogeneous co-localization of all five elements (Figure S18).

The data discussed above indicate that, under these reaction conditions, Sn by itself does not result in the formation of nanoparticles, but the slow injection of the noble metals in the presence of heated dissolved $SnCl_2$ results in the immediate formation of nanoparticles. A time dependent study of this sequential injection process (Figures S16 and S17) revealed that the early time points (1 min after addition of the noble metals) consist of Sn-rich PdSn (~22% Pd and 58% Sn) nanoparticles that also contain ~12% Pt and a smaller amount of Ir (~7%). As the reaction progresses (2.5 min), the Sn concentration drops while additional Rh incorporates. The rest of the metals maintain nearly constant concentrations. As the reaction progresses further, the Sn concentration continues to drop while the Pd concentration increases, and then the Pd concentration decreases while Pt, Rh and Ir incorporate. Finally, Sn, Pd, Pt, and Ir equilibrate to near-equimolar ratios while Rh remains consistently lower (~10-12%). Reversing the sequence of injection, *i.e.*, adding $SnCl_2$ after the four noble metal salts were added, also results in the formation of HEA nanoparticles (Figure S18).

The experiments described above provide two key insights. First, the presence of dissolved $SnCl_2$ during the stage of the reaction when the noble metal salts are reduced is crucial for the formation

of compositionally homogeneous HEA nanoparticles. Second, sequential injection leads to the formation of HEA nanoparticles *via* a PdSn seed mediated pathway, but simultaneous injection does not appear to form any nanoparticle seeds. Thus, simultaneous injection in the SnPdPtRhIr system likely proceeds through co-reduction and rapid mixing of all five metals to form the HEA nanoparticles. This reaction pathway is therefore distinctly different from the seed mediated pathway observed for NiPdPtRhIr. The presence of five different metals, including from both the d-block and the p-block, appears to help modulate the chemical reactivity and reduction kinetics in complex and interrelated ways. The presence of multiple metals in the reaction at the same time also influences crystal structure, composition, and nanoparticle formation, as is evident from control experiments (for analogous reactions involving only one metal) where we observe the formation of Ni_3C instead of Ni and the lack of formation of Rh and Ir nanoparticles. Sn has a different crystal structure than the 3d transition metals and, when combined with 3d transition metals in binary compounds, tends to form ordered intermetallic compounds rather than solid-solution alloys. Our observations suggest that Pd may serve as a template to help balance chemical reactivity, reduction kinetics, and possibly even crystal structure, given the incorporation of Sn into the face-centered cubic HEA. However, we do not yet have a full understanding of how all of these factors interrelate, given the compositional complexity of the system, the incorporation of both d-block and p-block metals, and the nature of the simultaneous multi-metal reactions. Preliminary reactions involving Pb, Bi, and Sb under analogous conditions did not initially lead to the formation of a complex solid solution, which motivates further studies aimed at expanding the compositional space of the colloidal HEA nanoparticles and understanding at a deeper level the reaction parameters and pathway that lead to their formation.

NiPdPtRhIr and SnPdPtRhIr, which differ only by the identity of the non-noble metal (Ni *vs* Sn), represent two distinct pathways for forming colloidal HEA nanoparticles: NiPdPtRhIr forms a nanoparticle seed as an intermediate and SnPdPtRhIr forms directly through simultaneous co-reduction of all elements. We were therefore interested in understanding how NiSnPdPtIr forms, as it contains both Ni and Sn and therefore represents a possible competition between two distinct pathways. The data in Figure 8 suggest that NiSnPdPtIr forms through a subtle combination of both seed-mediated and co-reduction approaches. At 1 min into the reaction, the isolated particles were highly deficient in Ni (~4%) and rich in Pd (33%), while Sn, Pt and Ir were each present at levels of approximately 24%, 18%, and 20%, respectively (Figures 8 and S19). With time the Ni concentration gradually increased while the Pd concentration decreased before leveling out to near equimolar concentrations (Figures 8, S19 and S20). Thus, the presence of Sn most likely triggered the immediate and rapid reduction of all noble metal salts, which inhibited the formation of NiPd seeds. However, the higher concentration of Pd relative to the other metals early in the reaction hints at a competition with the pathway that forms Pd-rich seeds. Thereafter, more Ni is incorporated at the expense of Pd, resulting in the final composition of $Ni_{0.15}Sn_{0.23}Pd_{0.20}Pt_{0212}Ir_{0.21}$, based on analysis of the EDS data in Figures 8 and S20. The NiSnPdPtIr alloy has a = 3.91 Å, which is slightly smaller than the weighted average of the constituent metals, a = 4.00 Å. However, the lattice constant for NiSnPdPtIr is larger than those for the HEAs that do not contain Sn and smaller than for SnPdPtRhIr, which does not contain Ni.

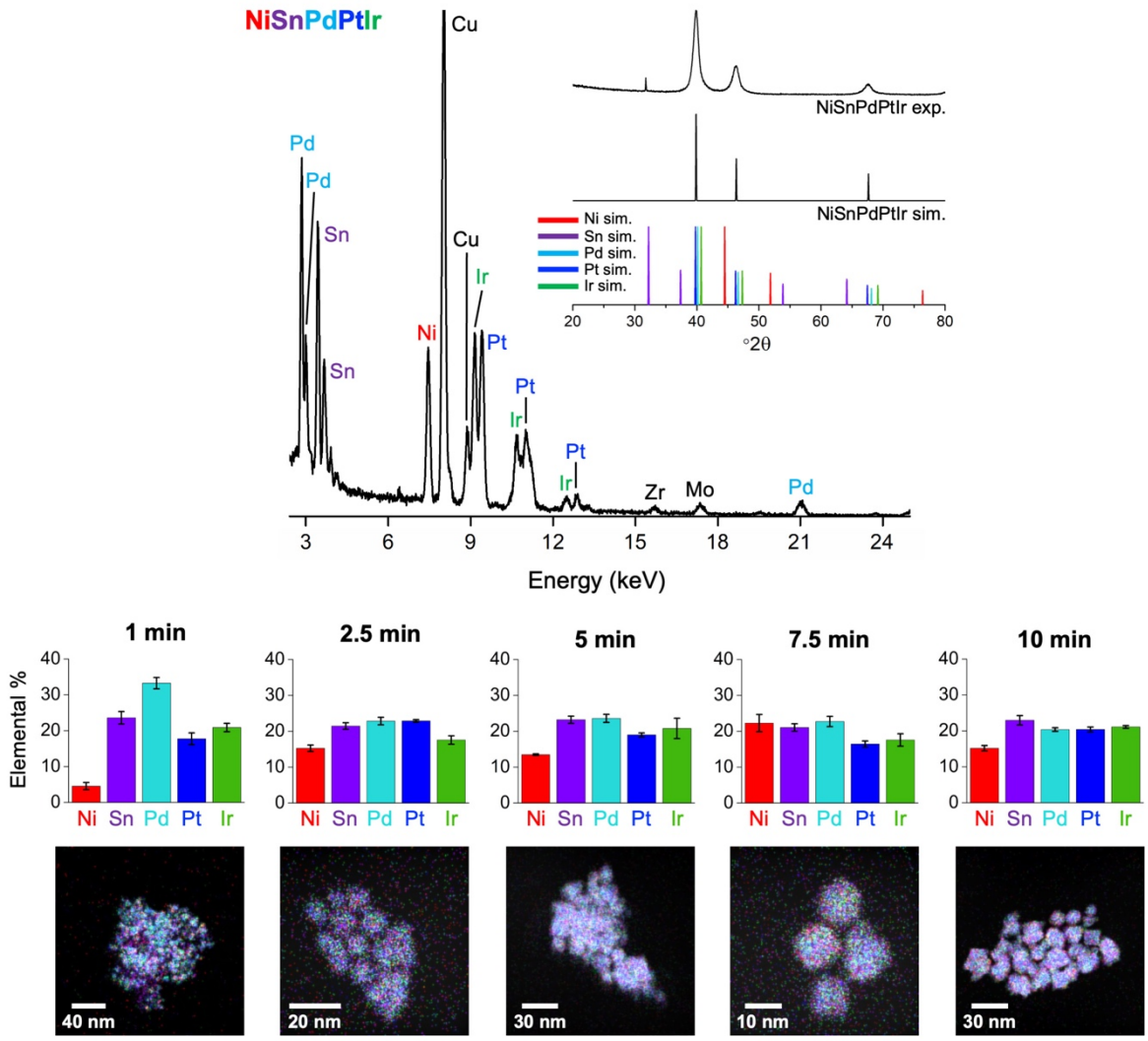

Figure 8. Characterization and time dependent formation of NiSnPdPtIr. An ensemble EDS spectrum and powder XRD pattern (Cu Kα radiation) are shown at the top. The EDS spectrum confirms the presence of all five elements in the sample. The Cu signal is from the Cu TEM grid, the Mo signal is from the Mo clips used in the TEM holder, and Zr is from the instrument. The XRD pattern confirms the formation of a single-phase fcc alloy. A simulated fcc XRD pattern, along with reference XRD patterns for each individual element, are provided for comparison. The sharp peak in the XRD pattern around 32 º2θ is an artifact from the XRD plate. At the bottom, bar charts of EDS elemental composition are shown, along with corresponding STEM-EDS element maps (Ni Kα, red; Sn Lα, purple; Pd Lα, cyan; Pt Lα, blue; Ir Lα, green). The time evolution is shown through the STEM-EDS maps, leading to nanoparticles having a final composition of $Ni_{0.15}Sn_{0.23}Pd_{0.20}Pt_{0.21}Ir_{0.21}$.

CONCLUSIONS

In conclusion, we have demonstrated the direct colloidal synthesis of seven HEA nanoparticle systems – NiPdPtRhIr, FePdPtRhIr, CoPdPtRhIr, NiFePdPtIr, NiFeCoPdPt, SnPdPtRhIr, and NiSnPdPtIr – that contain various combinations of noble metals, 3d transition metals, and a p-block element. Studies that varied key reaction parameters provided practical insights into how to

target conditions that most effectively incorporate the desired elements, in the desired ratios, into the HEA nanoparticles. This is important knowledge for advancing the rational synthesis of HEA nanoparticles, given the widely different reduction potentials, reduction kinetics, and decomposition temperatures that are inherent in five-metal systems. Reaction conditions must subtly balance competing factors that lead to phase segregations so that formation of compositionally homogeneous HEAs is favored. Additionally, time-dependent studies provided glimpses of how the HEA nanoparticle formation reactions proceed, including how and when various elements are introduced and how they are spatially distributed. For the all-transition metal systems, the initial formation of Pd-rich seeds, including NiPd in the Ni-containing systems, is notable, as it provides a reactive synthon that can facilitate reduction and/or deposition through galvanic and/or autocatalytic processes. However, this pathway is not broadly generalizable, as analogous studies on the SnPdPtRhIr and NiSnPdPtIr systems instead indicated HEA nanoparticle formation *via* simultaneous reduction and mixing of all metals, facilitated by the presence of Sn.

Throughout all of these reactions, it was clear that the pathways are often different depending on the elements and various reaction parameters, but the systems studied are capable of converging as HEAs. Complex system-dependent reaction pathways are therefore operable during the direct synthesis of colloidal HEA nanoparticles and subtle changes in the reaction protocol or choice of constituent elements can significantly change the process and outcome. Further work is needed to identify and understand a broader scope of reaction pathways, including the interplays among different metals and their effects on the formation of HEA nanoparticles, for a larger number of multi-element systems. Moreover, it will be important to understand how rigorous composition control can be achieved, including tunable element ratios, as this capability will allow the properties of HEA nanoparticles to be fine-tuned. Finally, while achieving size and shape control was not within the scope of this study, the knowledge that it generated is a stepping-stone to accessing desired morphological features.

EXPERIMENTAL SECTION

Chemicals

Octadecene [ODE, 90%, technical grade] and technical grade oleylamine [tg-OLAM, 70%] were purchased from Sigma-Aldrich. Nickel(II) acetylacetonate [$Ni(acac)_2$, 95%], cobalt(III) acetylacetonate [$Co(acac)_3$, 98%], palladium(II) acetylacetonate [$Pd(acac)_2$, 99%], rhodium(III) acetylacetonate [$Rh(acac)_3$, 97%], and tin(II) chloride [$SnCl_2$, reagent grade, 98%] were purchased from Sigma-Aldrich. Iron(III) acetylacetonate [$Fe(acac)_3$], platinum(II) acetylacetonate [$Pt(acac)_2$, ≥48.0% Pt], and iridium(IV) chloride [$IrCl_4$, ≥56.5% Ir] were purchased from Alfa Aesar. All solvents, including hexanes, toluene, and acetone, were of analytical grade. All the above chemicals were used as received without further purification.

Synthesis of HEA nanoparticles

Precursor solutions of $Ni(acac)_2$, $Fe(acac)_3$, $Co(acac)_3$, $Pd(acac)_2$, $Pt(acac)_2$, $Rh(acac)_3$, $IrCl_4$, and $SnCl_2$ were prepared by dissolving 13.54 mg, 18.61 mg, 18.77 mg, 16.05 mg, 20.73 mg, 21.09 mg, 17.60 mg, and 9.99 mg of the respective salts, respectively, in 5 mL of tg-OLAM. Note that the metal salts were chosen based on ease of use and literature precedent; most are acac salts except for tin and iridium, where chlorides were used. $SnCl_2$ is a well-known reagent used to synthesize Sn nanoparticles.[46,47,] Ir nanoparticles in the literature are often synthesized from chloride salts.[48,49,] A combination of heating (80 ºC – 120 ºC), stirring, and sonication was used to ensure the complete dissolution of the salts in tg-OLAM. Thereafter, depending on the constituent metals of the target HEA, 800 µL of each of the respective precursor solutions were mixed in a septum capped vial and made up to 4 mL using tg-OLAM wherever required. This

precursor solution mixture was placed under vacuum and held for 15 mins while stirring. The vial was then placed under Ar after cycling the vial between vacuum and Ar three times.

Meanwhile, 10 mL of ODE and 6 mL of tg-OLAM were combined in a 50 mL 3-neck round bottom flask with a reflux condenser, thermocouple attached to an adapter, gas flow adapter, rubber septum, and a magnetic stir bar. The flask was placed under vacuum, heated to 120 ºC, and held for 30 min before being cycled between vacuum and Ar three times. The flask under Ar was then heated to the appropriate reaction temperature. For slow injections, the precursor solution mixture was then injected slowly over 10 min at a rate of 0.4 mL/min into the solvent flask at the reaction temperature. For rapid injections, the precursor solution mixture was injected rapidly and held for 1 h. At the end of the reaction time, the flask was allowed to cool down to 200 ºC before quenching in a water bath. The product was isolated by washing the particles with toluene and acetone in a ratio of 1:4 followed by centrifugation and resuspension in toluene. The washing step was carried out three times in total and the final product was suspended in toluene. NiPdPtRhIr, SnPdPtRhIr, and SnNiPdPtIr were synthesized by slow injection at 275 ºC over 10 min. FePdPtRhIr, CoPdPtRhIr, and NiFePdPtIr were synthesized by rapid injection at 315 ºC and holding the reaction for 1 h. NiFeCoPdPt was synthesized by slow injection at 315 ºC over 10 min.

Annealing NiPdPtRhIr

$Ni_{0.19}Pd_{0.21}Pt_{0.22}Rh_{0.20}Ir_{0.18}$ nanoparticles (approx. 3 mg) were suspended in hexanes and dropcast on a silicon wafer. The wafer was then flame sealed in a quartz ampule under a pressure of 20 mTorr and placed in a furnace at room temperature. The furnace was heated at a ramp rate of 10 ºC/min to 800 ºC and held for 24 h before allowing it to naturally cool to room temperature in the furnace.

Characterization

A Malvern PANalytical Empyrean III using Cu Kα radiation was used to collect powder X-ray diffraction (XRD) data. A FEI Tecnai G20 20 XTWIN microscope operating at 200 kV was used to collect transmission electron microscopy (TEM) images. A FEI Talos F2000X S/TEM operating at an accelerating voltage of 200 kV was used to collect high resolution TEM (HRTEM) images, high angle annular dark field scanning TEM (HAADF-STEM) images, and STEM energy dispersive X-ray spectroscopy (STEM-EDS) maps. ImageJ was used to analyze the HRTEM images. Bruker ESPRIT 1.9 software was used to interpret the STEM-EDS element map data. The EDS lines mapped were Ni Kα, Fe Kα, Co Kα, Sn Lα, Pd Lα, Pt Lα, Rh Lα, and Ir Lα. EDS quantification was done using Ni Kα, Fe Kα, Co Kα, Sn Lα, Pd Kα, Pt Lα, Rh Kα, and Ir Lα lines. The low energy Pd Lα and Rh Lα energy lines (2.838 keV and 2.696 keV respectively) are very close to each other and overlap slightly. Therefore, the higher energy Kα lines (21.177 keV for Pd and 20.216 for Rh), which are widely spaced and do not overlap, were used to minimize quantification errors. All crystal structures shown were generated using CrystalMaker and all simulated diffraction patterns were generated using CrystalDiffract. Both are distributed by CrystalMaker Software Ltd., Oxford, England (www.crystalmaker.com)

ASSOCIATED CONTENT

Supporting Information

The Supporting Information is available free of charge on the ACS Publications website.

- Additional XRD, EDS, TEM, and time-dependent STEM-EDS data, as well as information about lattice parameter calculations.

AUTHOR INFORMATION

Corresponding Author
* res20@psu.edu

Notes
The authors declare no competing financial interest.

ACKNOWLEDGMENT

This work was supported by the U.S. National Science Foundation under grant CHE-2203353. TEM and XRD data were acquired at the Materials Characterization Lab of the Penn State Materials Research Institute.

REFERENCES

(1) Yeh, J. W.; Chen, S. K.; Lin, S. J.; Gan, J. Y.; Chin, T. S.; Shun, T. T.; Tsau, C. H.; Chang, S. Y. Nanostructured High-Entropy Alloys with Multiple Principal Elements: Novel Alloy Design Concepts and Outcomes. *Adv. Eng. Mater.* **2004**, *6* (5), 299–303.

(2) Cantor, B.; Chang, I. T. H.; Knight, P.; Vincent, A. J. B. Microstructural Development in Equiatomic Multicomponent Alloys. *Mater. Sci. Eng. A* **2004**, *375–377*, 213–218.

(3) George, E. P.; Raabe, D.; Ritchie, R. O. High-Entropy Alloys. *Nat. Rev. Mater.* **2019**, *4* (8), 515–534.

(4) Praveen, S.; Kim, H. S. High-Entropy Alloys: Potential Candidates for High-Temperature Applications – An Overview. *Adv. Eng. Mater.* **2018**, *20* (1), 1700645.

(5) Wang, X.; Yao, H.; Zhang, Z.; Li, X.; Chen, C.; Yin, L.; Hu, K.; Yan, Y.; Li, Z.; Yu, B.; Cao, F.; Liu, X.; Lin, X.; Zhang, Q. Enhanced Thermoelectric Performance in High Entropy Alloys Sn0.25Pb0.25Mn0.25Ge0.25Te. *ACS Appl. Mater. Interfaces* **2021**, *13* (16), 18638–18647.

(6) Kumari, P.; Gupta, A. K.; Mishra, R. K.; Ahmad, M. S.; Shahi, R. R. A Comprehensive Review: Recent Progress on Magnetic High Entropy Alloys and Oxides. *J. Magn. Magn. Mater.* **2022**, *554*, 169142.

(7) Xin, Y.; Li, S.; Qian, Y.; Zhu, W.; Yuan, H.; Jiang, P.; Guo, R.; Wang, L. High-Entropy Alloys as a Platform for Catalysis: Progress, Challenges, and Opportunities. *ACS Catal.* **2020**, *10* (19), 11280–11306.

(8) Sun, Y.; Dai, S. High-Entropy Materials for Catalysis: A New Frontier. *Sci. Adv.* **2021**, *7* (20), eabg1600.

(9) Löffler, T.; Savan, A.; Garzón-Manjón, A.; Meischein, M.; Scheu, C.; Ludwig, A.; Schuhmann, W. Toward a Paradigm Shift in Electrocatalysis Using Complex Solid Solution Nanoparticles. *ACS Energy Lett.* **2019**, *4* (5), 1206–1214.

(10) Yao, Y.; Huang, Z.; Xie, P.; Lacey, S. D.; Jacob, R. J.; Xie, H.; Chen, F.; Nie, A.; Pu, T.; Rehwoldt, M.; Yu, D.; Zachariah, M. R.; Wang, C.; Shahbazian-Yassar, R.; Li, J.; Hu, L. Carbothermal Shock Synthesis of High-Entropy-Alloy Nanoparticles. *Science* **2018**, *359* (6383), 1489–1494.

(11) Waag, F.; Li, Y.; Ziefuß, A. R.; Bertin, E.; Kamp, M.; Duppel, V.; Marzun, G.; Kienle, L.; Barcikowski, S.; Gökce, B. Kinetically-Controlled Laser-Synthesis of Colloidal High-Entropy Alloy Nanoparticles. *RSC Adv.* **2019**, *9* (32), 18547–18558.

(12) Wang, B.; Wang, C.; Yu, X.; Cao, Y.; Gao, L.; Wu, C.; Yao, Y.; Lin, Z.; Zou, Z. General Synthesis of High-Entropy Alloy and Ceramic Nanoparticles in Nanoseconds. *Nat. Synth.* **2022**, *1* (2), 138–146.

(13) Liu, M.; Zhang, Z.; Okejiri, F.; Yang, S.; Zhou, S.; Dai, S. Entropy-Maximized Synthesis of Multimetallic Nanoparticle Catalysts via a Ultrasonication-Assisted Wet Chemistry Method under Ambient Conditions. *Adv. Mater. Interfaces* **2019**, *6* (7), 1900015.

(14) Löffler, T.; Meyer, H.; Savan, A.; Wilde, P.; Garzón Manjón, A.; Chen, Y.-T.; Ventosa, E.; Scheu, C.; Ludwig, A.; Schuhmann, W.; Löffler, T.; Wilde, P.; Chen, Y.; Schuhmann, W.; Meyer, H.; Savan, A.; Ludwig, A.; Garzón Manjón, A.; Scheu, C.; Ventosa, E. Discovery of a Multinary Noble Metal–Free Oxygen Reduction Catalyst. *Adv. Energy Mater.* **2018**, *8* (34), 1802269.

(15) Yang, Y.; Song, B.; Ke, X.; Xu, F.; Bozhilov, K. N.; Hu, L.; Shahbazian-Yassar, R.; Zachariah, M. R. Aerosol Synthesis of High Entropy Alloy Nanoparticles. *Langmuir* **2020**, *36* (8), 1985–1992.

(16) Niu, B.; Zhang, F.; Ping, H.; Li, N.; Zhou, J.; Lei, L.; Xie, J.; Zhang, J.; Wang, W.; Fu, Z. Sol-Gel Autocombustion Synthesis of Nanocrystalline High-Entropy Alloys. *Sci. Reports* **2017**, *7* (1), 3421.

(17) Xia, Y.; Xia, X.; Peng, H. C. Shape-Controlled Synthesis of Colloidal Metal Nanocrystals: Thermodynamic versus Kinetic Products. *J. Am. Chem. Soc.* **2015**, *137* (25), 7947–7966.

(18) Ortiz, N.; Skrabalak, S. E. On the Dual Roles of Ligands in the Synthesis of Colloidal Metal Nanostructures. *Langmuir* **2014**, *30* (23), 6649–6659.

(19) You, H.; Yang, S.; Ding, B.; Yang, H. Synthesis of Colloidal Metal and Metal Alloy Nanoparticles for Electrochemical Energy Applications. *Chem. Soc. Rev.* **2013**, *42* (7),

(20) Xia, Y.; Xiong, Y.; Lim, B.; Skrabalak, S. E. Shape-Controlled Synthesis of Metal Nanocrystals: Simple Chemistry Meets Complex Physics? *Angew. Chemie Int. Ed.* **2009**, *48* (1), 60–103.

(21) Gilroy, K. D.; Ruditskiy, A.; Peng, H. C.; Qin, D.; Xia, Y. Bimetallic Nanocrystals: Syntheses, Properties, and Applications. *Chem. Rev.* **2016**, *116* (18), 10414–10472..

(22) Li, H.; Han, Y.; Zhao, H.; Qi, W.; Zhang, D.; Yu, Y.; Cai, W.; Li, S.; Lai, J.; Huang, B.; Wang, L. Fast Site-to-Site Electron Transfer of High-Entropy Alloy Nanocatalyst Driving Redox Electrocatalysis. *Nat. Commun.* **2020**, *11* (1), 1–9..

(23) Wu, D.; Kusada, K.; Yamamoto, T.; Toriyama, T.; Matsumura, S.; Kawaguchi, S.; Kubota, Y.; Kitagawa, H. Platinum-Group-Metal High-Entropy-Alloy Nanoparticles. *J. Am. Chem. Soc.* **2020**, *142* (32), 13833–13838.

(24) Chen, Y.; Zhan, X.; Bueno, S. L. A.; Shafei, I. H.; Ashberry, H. M.; Chatterjee, K.; Xu, L.; Tang, Y.; Skrabalak, S. E. Synthesis of Monodisperse High Entropy Alloy Nanocatalysts from Core@shell Nanoparticles. *Nanoscale Horizons* **2021**, *6* (3), 231–237.

(25) Moreira Da Silva, C.; Amara, H.; Fossard, F.; Girard, A.; Loiseau, A.; Huc, V. Colloidal Synthesis of Nanoparticles: From Bimetallic to High Entropy Alloys. *Nanoscale* **2022**, *14*

(27), 9832–9841.

(26) Broge, N. L. N.; Bondesgaard, M.; Søndergaard-Pedersen, F.; Roelsgaard, M.; Iversen, B. B. Autocatalytic Formation of High-Entropy Alloy Nanoparticles. *Angew. Chemie* **2020**, *132* (49), 22104–22108.

(27) Tao, L.; Sun, M.; Zhou, Y.; Luo, M.; Lv, F.; Li, M.; Zhang, Q.; Gu, L.; Huang, B.; Guo, S. A General Synthetic Method for High-Entropy Alloy Subnanometer Ribbons. *J. Am. Chem. Soc.* **2022**, *144* (23), 10582–10590.

(28) Sun, Y.; Zhang, W.; Zhang, Q.; Li, Y.; Gu, L.; Guo, S. A General Approach to High-Entropy Metallic Nanowire Electrocatalysts. *Matter* **2022**.

(29) Chen, Z.; Wen, J.; Wang, C.; Kang, X.; Chen, Z.; Wen, J.; Wang, C.; Kang, X. Convex Cube-Shaped Pt34Fe5Ni20Cu31Mo9Ru High Entropy Alloy Catalysts toward High-Performance Multifunctional Electrocatalysis. *Small* **2022**, *18* (45), 2204255.

(30) Bueno, S. L. A.; Leonardi, A.; Kar, N.; Chatterjee, K.; Zhan, X.; Chen, C.; Wang, Z.; Engel, M.; Fung, V.; Skrabalak, S. E. Quinary, Senary, and Septenary High Entropy Alloy Nanoparticle Catalysts from Core@Shell Nanoparticles and the Significance of Intraparticle Heterogeneity. *ACS Nano* **2022**, *16*, 18873–18885.

(31) Zhang, D.; Shi, Y.; Zhao, H.; Qi, W.; Chen, X.; Zhan, T.; Li, S.; Yang, B.; Sun, M.; Lai, J.; Huang, B.; Wang, L. The Facile Oil-Phase Synthesis of a Multi-Site Synergistic High-Entropy Alloy to Promote the Alkaline Hydrogen Evolution Reaction. *J. Mater. Chem. A* **2021**, *9* (2), 889–893.

(32) Zhang, D.; Zhao, H.; Wu, X.; Deng, Y.; Wang, Z.; Han, Y.; Li, H.; Shi, Y.; Chen, X.; Li, S.; Lai, J.; Huang, B.; Wang, L.; Zhang, D.; Zhao, H.; Wu, X.; Deng, Y.; Wang, Z.; Han, Y.; Li, H.; Shi, Y.; Lai, J.; Wang, L.; Chen, X.; Li, S.; Huang, B. Multi-Site Electrocatalysts Boost PH-Universal Nitrogen Reduction by High-Entropy Alloys. *Adv. Funct. Mater.* **2021**, *31* (9), 2006939.

(33) Zhan, C.; Xu, Y.; Bu, L.; Zhu, H.; Feng, Y.; Yang, T.; Zhang, Y.; Yang, Z.; Huang, B.; Shao, Q.; Huang, X. Subnanometer High-Entropy Alloy Nanowires Enable Remarkable Hydrogen Oxidation Catalysis. *Nat. Commun.* **2021**, *12* (1), 1–8.

(34) Singh, M. P.; Srivastava, C. Synthesis and Electron Microscopy of High Entropy Alloy Nanoparticles. *Mater. Lett.* **2015**, *160*, 419–422.

(35) Yu, Y.; Xia, F.; Wang, C.; Wu, J.; Fu, X.; Ma, D.; Lin, B.; Wang, J.; Yue, Q.; Kang, Y. High-Entropy Alloy Nanoparticles as a Promising Electrocatalyst to Enhance Activity and Durability for Oxygen Reduction. *Nano Res.* **2022**, *15* (9), 7868–7876.

(36) Fu, X.; Zhang, J.; Zhan, S.; Xia, F.; Wang, C.; Ma, D.; Yue, Q.; Wu, J.; Kang, Y. High-Entropy Alloy Nanosheets for Fine-Tuning Hydrogen Evolution. *ACS Catal.* **2022**, *12* (19), 11955–11959.

(37) Mourdikoudis, S.; Liz-Marzán, L. M. Oleylamine in Nanoparticle Synthesis. *Chem. Mater.* **2013**, *25* (9), 1465–1476.

(38) Wu, Y.; Wang, D.; Zhao, P.; Niu, Z.; Peng, Q.; Li, Y. Monodispersed Pd-Ni Nanoparticles: Composition Control Synthesis and Catalytic Properties in the Miyaura-Suzuki Reaction. *Inorg. Chem.* **2011**, *50* (6), 2046–2048.

(39) Shviro, M.; Polani, S.; Dunin-Borkowski, R. E.; Zitoun, D. Bifunctional Electrocatalysis on

Pd-Ni Core–Shell Nanoparticles for Hydrogen Oxidation Reaction in Alkaline Medium. *Adv. Mater. Interfaces* **2018**, *5* (9), 1701666..

(40) Xia, X.; Wang, Y.; Ruditskiy, A.; Xia, Y.; Xia, X.; Wang, Y.; Xia, Y.; Ruditskiy, A. 25th Anniversary Article: Galvanic Replacement: A Simple and Versatile Route to Hollow Nanostructures with Tunable and Well-Controlled Properties. *Adv. Mater.* **2013**, *25* (44), 6313–6333.

(41) Huang, X.; Zhang, H.; Guo, C.; Zhou, Z.; Zheng, N.; Huang, X. Q.; Zhang, H. H.; Guo, C. Y.; Zhou, Z. Y.; Zheng, N. F. Simplifying the Creation of Hollow Metallic Nanostructures: One-Pot Synthesis of Hollow Palladium/Platinum Single-Crystalline Nanocubes. *Angew. Chemie Int. Ed.* **2009**, *48* (26), 4808–4812.

(42) Pham, V. V.; Ta, V. T.; Sunglae, C. Synthesis of NiPt Alloy Nanoparticles by Galvanic Replacement Method for Direct Ethanol Fuel Cell. *Int. J. Hydrogen Energy* **2017**, *42* (18), 13192–13197.

(43) Park, K. H.; Jang, K.; Kim, H. J.; Son, S. U. Near-Monodisperse Tetrahedral Rhodium Nanoparticles on Charcoal: The Shape-Dependent Catalytic Hydrogenation of Arenes. *Angew. Chemie Int. Ed.* **2007**, *46* (7), 1152–1155.

(44) Lide, D. R. *CRC Handbook of Chemistry and Physics, 89th Edition*; CRC Press, Taylor & Francis: Boca Raton, FL., 2008.

(45) *Materials Project.* https://materialsproject.org/materials/mp-1022725?chemsys=Sn#literature_references (accessed 2022-12-19), *Data retrieved from the Materials Project for Sn (mp-1022725) from database version v2021.11.10.*

(46) Zhao, X.; Yang, Q.; Quan, Z. Tin-Based Nanomaterials: Colloidal Synthesis and Battery Applications. *Chem. Commun.* **2019**, *55* (60), 8683–8694.

(47) Kravchyk, K.; Protesescu, L.; Bodnarchuk, M. I.; Krumeich, F.; Yarema, M.; Walter, M.; Guntlin, C.; Kovalenko, M. V. Monodisperse and Inorganically Capped Sn and Sn/SnO2 Nanocrystals for High-Performance Li-Ion Battery Anodes. *J. Am. Chem. Soc.* **2013**, *135* (11), 4199–4202.

(48) Mathiesen, J. K.; Quinson, J.; Blaseio, S.; Kjær, E. T. S.; Dworzak, A.; Cooper, S. R.; Pedersen, J. K.; Wang, B.; Bizzotto, F.; Schröder, J.; Kinnibrugh, T. L.; Simonsen, S. B.; Theil Kuhn, L.; Kirkensgaard, J. J. K.; Rossmeisl, J.; Oezaslan, M.; Arenz, M.; Jensen, K. M. Ø. Chemical Insights into the Formation of Colloidal Iridium Nanoparticles from In Situ X-Ray Total Scattering: Influence of Precursors and Cations on the Reaction Pathway. *J. Am. Chem. Soc.* **2023**, *145* (3), 1769–1782.

(49) Fu, L.; Cai, P.; Cheng, G.; Luo, W. Colloidal Synthesis of Iridium-Iron Nanoparticles for Electrocatalytic Oxygen Evolution. *Sustain. Energy Fuels* **2017**, *1* (5), 1199–1203.

Table of Contents Graphic